PNAS
www.pnas.org

Supplementary Information for

Large H_2O Solubility in Dense Silica and its Implications for the Interiors of Water-Rich Planets

Carole Nisr, Huawei Chen, Kurt Leinenweber, Andrew Chizmeshya, Vitali Prakapenka, Clemens Prescher, Sergey Tkachev, Yue Meng, Zhenxian Liu, Sang-Heon Shim

Sang-Heon Shim.
E-mail: shdshim@gmail.com

This PDF file includes:

www.pnas.org/cgi/doi/10.1073/pnas.1917448117

Supporting Information Text

1. Identification of the Ct phase

The most notable diagnostic feature of Ct is 121_{Ct} at ∼1.46 Å. The peak does not overlap with any of the lines from Stv (Fig. 1). The 110_{Ct}, 211_{Ct}, and 220_{Ct} lines appear as peak splitting of the 110_{Stv}, 211_{Stv}, and 220_{Stv} lines when the Ct phase exist. The 111_{Stv} and 121_{Ct} lines are the most diagnostic features for the presence of Stv and the Ct phases, respectively. The 111_{Stv} is close but does not overlap with 111_{Ct} because the 111_{Ct} line shifts away from 111_{Stv} from the strong distortion constrained by the 121_{Ct} position. The 111_{Ct} overlaps with an Au peak.

Based on these criteria, we identified the phases in the Peakpo software (1) by adjusting the unit-cell volume and axial ratios. Such adjustments normally distinguished the two phases. However, due to the overlapping lines of these two phases, we do not rule out the possibility that the Ct phase has an even lower symmetry than orthorhombic.

We also attempted to fit all the observed silica diffraction lines to a single crystal structure. However, none of the crystal structures in the rutile-related materials we tested could explain all the diffraction peaks together. We tried a $CoReO_3$-type structure (orthorhombic $Cmmm$), a tilted stishovite type, a VO_2-type (monoclinic $P2_1/c$), as well as the simple shear distorted versions of the structures, and a twisted $CoReO_4$ model. The new lines could be explained best with a two phase mixture: Stv and the $CaCl_2$ type (Ct). We used the 111_{Stv} peak at ∼1.93 Å (Fig. 1a) as the diagnostic line of Stv. The presence of the shoulders at the 110, 211, and 220 peaks (at ∼2.88 Å, ∼1.49 Å, and ∼1.43 Å, respectively) in the diffraction patterns (Fig. 1a) could also confirm the presence of Stv.

2. Infrared spectroscopy of OH in silica

The IR spectra from all the samples measured revealed pronounced peaks in the OH stretching region between 2400 and 3800 cm^{-1} (Fig. 2 inset and SI Fig. S1). For example, SI Fig. S1 shows the IR spectrum of the recovered sample synthesized from a dry stishovite + H_2O starting materials at 51 GPa and 2086 K. Although this sample contains the lowest amount of H_2O among the Ct samples (0.4 wt% H_2O), the IR spectrum showed clear OH bands.

The shape of the OH band from Ct suggests that it consists of at least 3–5 peaks, which as also found in Raman spectra (2) and IR spectra (3) previously reported on hydrous Stv. The peak positions of the lower-frequency features in hydrous Stv are within the variation we found among our hydrous Ct samples. However, the intensity distribution among the peaks is noticeably different. For example, while the ~3200 cm^{-1} is more pronounced in our spectra, the peak only exists as a shoulder feature in hydrous Stv. It is important to note that our Ct sample in general contains more H_2O than the reported spectrum for Stv (~1.3 wt% H_2O) (3). Furthermore, our samples are hydrous Stv converted from Ct while the samples in ref. 3 were from hydrous Stv.

The features found in the IR spectra of our samples are within a similar spectral range as the OH modes observed for hydrous ringwoodite samples (4, 5), although there are some important differences in the spectra because of the structural differences between stishovite and ringwoodite.

3. Estimation of H_2O content

For Stv synthesized at 9 GPa and low temperatures in the multi-anvil press, Spektor et al. (3, 6) found a linear relationship between the volume expansion and H_2O content. In their dataset, five samples have the H_2O content measured directly from thermogravimetric analysis (TGA). They also reported the unit-cell volumes of these five samples from X-ray diffraction. Later, Nisr et al. (2) fit the relationship between the H_2O content and the volume expansion of Stv to a line using these five well characterized samples (Fig. 2b), providing a way to estimate the H_2O content from the measured volume expansion.

4. First-principles calculations

GGA is known to correctly predict the structural energy differences for a range of silica polymorphs with different local environment, including coordination numbers (7). It is known that LDA yields physical properties of silica more consistent with experimentally measured values, including unit-cell volume and bulk modulus. We found that the unit-cell volume of anhydrous Ct from GGA is 5% higher than that of the experimentally reported value (8), similar to previously found for GGA (7). For LDA, our unit-cell volumes for the anhydrous models (dCt8 and dCt12) are in agreement with experimentally reported value within 0.2%. Yet it is important to note that the experimentally measured volume is measured at 300 K while the volumes from DFT are at 0 K. The thermal expansion expected between 0 and 300 K is 0.4%. The unit-cell volumes from the dCt8 and dCt12 models are essentially identical to each other.

Si defects (or H sites) are likely disordered in the experimentally observed Ct phase, because we do not have any evidence for super-lattice diffraction lines. However, in our DFT, the Si defects (or H sites) are ordered. To reduce artifacts due to the Si defect ordering, we constrained all three angles of the supercells to be 90° in the simulations. We also ran simulations without this constraint and found that the angles deviate from 90° for less than 0.5°. We found that the $CaCl_2$ type structure converts to rutile-type structure at 1 bar optimization, consistent with our experimental results.

We found that the unit-cell volume of Ct increases linearly with the concentration of H_2O in the crystal structure in both Ct8 and Ct12 simulations. In addition, despite the difference in cell setup, both model groups (Ct8 and Ct12) are in excellent agreement with each other. The linear trend can be also postulated for individual model sets (Ct8 and Ct12) independently, suggesting that the linear trend is not model dependent. We found some differences in the slope of the linear trend between GGA and LDA. The experimental data points are located between the GGA and LDA trends, as expected.

We found that the relationship between unit-cell volume expansion and c/a ratios is also linear similar to what was found in experimental data (SI Fig. S3). However, there are some differences as well, particularly noticeable at higher H_2O content. This is likely because of non-random distribution of Si defects (or H sites) in our DFT models.

5. Challenges associated with water content estimations based on IR

The integrated intensity of IR-active OH modes has been used to estimate the amounts of H_2O for some minerals (9, 10). Such method should be carefully applied because the frequency and the intensity of the OH modes change sensitively to the difference in the local structure near H atoms. Although some efforts have been made for such IR methods for hydrous Stv (11), the calibration was made for Stv with a significant amount of Al. Furthermore, the presented spectra for their calibration is significantly different from those of our Al-free dense silica, suggesting fundamental difference in the local structure of the H atoms and therefore preventing us from adapting the method. The most severe problem of applying the methods to the LHDAC sample is that the thickness of the sample is very difficult to measure. Although the samples were cold compressed to make thin and well-packed polycrystalline foils, we found that after recovery from LHDAC runs, the samples were no longer well-packed and even porous, likely because of the hydrothermal reaction. Therefore, it is very difficult to obtain reliable thickness. Despite the uncertainty, we found that application of Paterson's method (9) yields similar values as ones presented in SI tab. S1, if we assume a thickness of 5–10 microns.

6. Provisional phase diagram of SiO_2–H_2O

We observed that stable phases change with pressure in the SiO_2–H_2O system as a function of pressure. Therefore, it is of interest to build a phase diagram in $P-X(H_2O)$ where $X(H_2O)$ is molar content of H_2O in SiO_2. Because we have estimates for the content of H_2O for Ct, here we focus more on the lower pressure regime for the provisional phase diagram (Fig. 3b). Because of a range of temperatures in our data, we focus on 1400–1500 K and compare the result with a few data points at 1700 K and 900 K (Fig. 3b).

To constrain the stability field of pure Stv and Ct phases, we use two data points: one multi-anvil data point at 10 GPa and 1500 K shows the stability of pure Stv with a low H_2O content, while at 45 GPa and 1740 K we found the stability of pure Ct with a large H_2O content in an LHDAC experiments. We then use two LHDAC data points where we found two Stv phases with different H_2O in the recovered samples from Ct + Stv at high pressure. These two data points provide constraints for the mixed phase region in the phase diagram. Because of the large uncertainties in $X(H_2O)$ from LHDAC and paucity of data points, we found it is difficult to fit to a single trend. However, a high-precision data point obtained from multi-anvil press at 20 GPa and 900 K supports the inferred phase boundaries in the diagram. The phase fields involving Nt is largely hypothesized from our H_2O estimations (see the main text) and experimental observations.

7. Equation of state of the Nt phase

We obtained the unit-cell volumes of the Nt phase from diffraction patterns measured during decompression. The unit-cell volumes were calculated from at least 3 or 4 diffraction lines for the hexagonal unit cell. We fit the unit-cell volumes of the Nt phase to the second order Birch–Murnaghan equation. In the fitting, we fixed the volume at 1.3 GPa (the lowest pressure data point) to a measured value. The pressure derivative of bulk modulus was fixed to 4 in the fitting.

Table S1. Experimental conditions, observed phases, and H_2O content for dense hydrous silica polymorphs. **Pressure (P) and temperature (T) are averages of the values measured during the heating cycles. Pressures at high temperatures are calculated from the measured unit-cell volumes of Au or Pt combined with their P–V–T equations of state (12). H_2O contents were estimated combined with the measured unit-cell volumes in table S2. SM: starting materials, hGel: hydrous silica gel, dGla: anhydrous silica glass, dStv: anhydrous stishovite, Calib.: pressure calibrants, Initial: phases observed at the initial stage of heating, Final: phases observed at the final stage of heating, Quench: phases in the quenched samples, Stv: stishovite, Ct: $CaCl_2$-type silica phase, and Nt: NiAs-type silica phase.**

Run	SM	Medium	Calib.	Dur. (min)	P (GPa)	T (K)	Initial	Final	Quench	H_2O (wt%)
512	dGla	H_2O	Pt	12	24.0(23)	1452(100)	Stv	Ct, Stv	Stv	8.4(11)
	dGla	H_2O	Pt	12	24.0(23)	1452(100)	Stv	Ct, Stv	Stv	1.1(2)
502	dGla	H_2O	Pt	10	48.0(6)	1464(100)	Ct, Stv	Ct, Stv	Stv	7.7(10)
	dGla	H_2O	Pt	10	48.0(6)	1464(100)	Ct, Stv	Ct, Stv	Stv	2.0(3)
618	dGla	H_2O	Pt	25	65.0(51)	1997(191)	Ct, Stv	Nt, Ct, Stv	Stv	5.6(7)
319	dGla	H_2O	Pt	10	67.0(20)	1911(100)	Nt, Ct, Stv	Nt, Ct, Stv	Stv	5.2(7)
404	hGel	Ne	Au	33	45.0(15)	1740(100)	Ct, Stv	Ct	Stv, Ct	7.1(9)
402	hGel	Ar	Au	24	59.0(14)	1564(100)	Nt	Nt		
303	hGel	Ne	Pt	5	56.0(4)	1506(100)	Ct, Stv	Ct, Stv	Stv	3.5(5)
119a	hGel	Ar	Pt	10	59.0(18)	1998(100)	Nt, Stv	Nt, Ct, Stv	Stv	2.1(3)
603	hGel	Ne	Pt	5	42.0(4)	1554(100)	Ct, Stv	Ct, Stv	Stv	1.1(2)
119b	dStv	H_2O	Pt	10	51.0(23)	2086(269)	Ct, Stv	Ct, Stv	Stv	0.4(1)
MB102	hGel	None	Pt	15	96.0(42)	2077(100)	Nt, Ct	Nt, Ct		
MB202	hGel	H_2O	Au	15	107.0(15)	1736(164)	Nt	Nt	Nt	
MB317	dGla	H_2O	Au	12	87.0(18)	1679(178)	Nt	Nt		
MB308	dGla	H_2O	Au	33	82.0(8)	1617(182)	Nt	Nt		
MB402	dGla	H_2O	Pt	16	64.0(15)	1699(100)	Nt	Nt		
MB602	hGel	H_2O	Au	12	111.0(14)	1700(141)	Nt	Nt		

Table S2. The unit-cell parameters of the stishovite phase at 1 bar and 300 K after recovery from high-pressure experiments. **For runs 512, 502, and Samp5, we detected two different Stv phases with different unit-cell volumes. The numbers in the parentheses are the estimated 1σ uncertainties.**

Run	a_0 (Å)	c_0 (Å)	V_0 (Å^3)
512	4.2550(11)	2.6697(33)	48.34(5)
	4.1888(11)	2.6651(20)	46.76(3)
502	4.2497(10)	2.6671(20)	48.17(3)
	4.1962(10)	2.6663(20)	46.95(3)
618	4.2299(10)	2.6672(7)	47.72(2)
319	4.2260(9)	2.6680(7)	47.65(2)
404	4.2451(10)	2.6660(8)	48.04(2)
303	4.2121(11)	2.6649(7)	47.28(2)
119a	4.1970(8)	2.6659(6)	46.96(2)
603	4.1880(9)	2.6659(13)	46.76(2)
119b	4.1816(9)	2.6652(7)	46.60(2)

Table S3. Unit-cell parameters of the niccolite-type silica phase at high pressure and 300 K. The numbers in the parentheses are the estimated 1σ uncertainties.

P (GPa)	a (Å)	c (Å)	V (Å^3)
93.0(12)	2.4029(6)	3.805(3)	19.02(1)
88.4(11)	2.4106(6)	3.814(3)	19.20(1)
80.8(10)	2.4196(6)	3.834(3)	19.44(1)
71.6(10)	2.4334(6)	3.849(3)	19.74(1)
54.6(8)	2.4741(6)	3.942(3)	20.90(1)
21.5(5)	2.5475(7)	4.087(3)	22.97(2)
1.3(3)	2.5848(7)	4.177(3)	24.17(2)

Table S4. The diffraction peak positions of the Ct silica phase and Stv at high pressures and 300 K. At 40.4 GPa and 300 K, we observed both Ct ($a = 4.143(3)$ Å, $b = 3.960(2)$ Å, $c = 2.519(2)$ Å) and Stv ($a = 4.051(1)$ Å, $c = 2.591(8)$ Å). At 36.9 GPa, we observed pure Ct ($a = 4.151(3)$ Å, $b = 3.970(3)$ Å, $c = 2.529(1)$ Å). hkl's are the Miller indices. $d_{\rm obs}$ and $d_{\rm cal}$ are the observed and calculated d-spacings, respectively, and Δd is the difference between them.

h	k	l	$d_{\rm obs}$ (Å)	$d_{\rm cal}$ (Å)	Δd (Å)
			Ct at 40.4 GPa		
1	1	0	2.8618	2.8628	−0.0010
0	2	0	1.9811	1.9800	0.0011
1	1	1	1.8907	1.8913	−0.0006
2	1	1	1.4844	1.4836	0.0008
1	2	1	1.4570	1.4573	−0.0003
2	2	0	1.4310	1.4314	−0.0004
			Stv at 40.4 GPa		
1	0	1	2.1805	2.1829	−0.0024
1	1	1	1.9220	1.9216	0.0004
2	1	0	1.8120	1.8115	0.0005
0	0	2	1.2958	1.2957	0.0001
3	1	0	1.2805	1.2809	−0.0005
2	2	1	1.2539	1.2534	0.0005
			Ct at 36.9 GPa		
1	1	0	2.8659	2.8689	−0.0030
1	0	1	2.1594	2.1596	−0.0002
1	1	1	1.8967	1.8971	−0.0004
2	1	1	1.4877	1.4874	0.0003
1	2	1	1.4617	1.4614	0.0003
2	2	0	1.4346	1.4344	0.0002

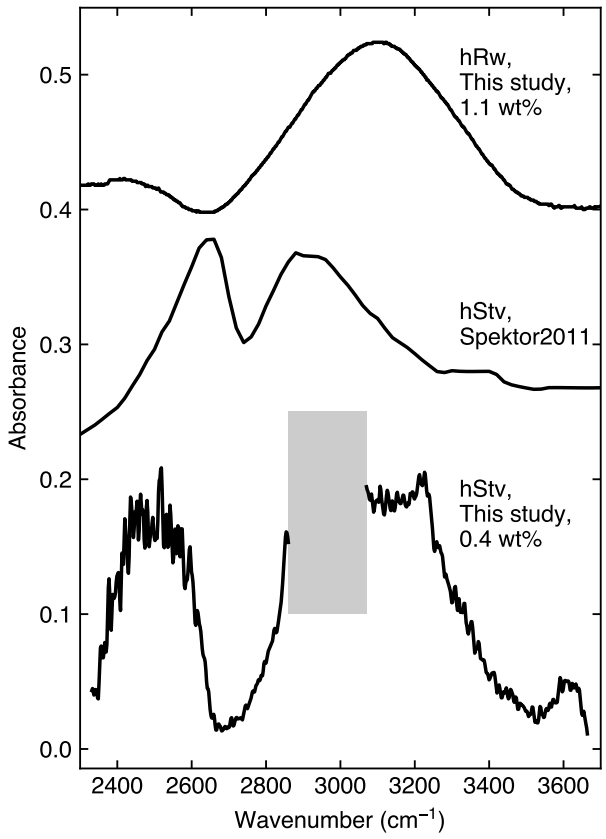

Fig. S1. **Infrared spectrum of hydrous dense silica synthesized from an anhydrous Stv + H_2O starting mixture at 51 GPa and 2086 K.** We compare the spectrum with hydrous Stv (3) and hydrous ringwoodite. We grayed area between 2850 and $3100\,\mathrm{cm}^{-1}$ because of extra features from the optics of the beamline system (13). Note that the measurement conditions, including the thickness of the samples, are different.

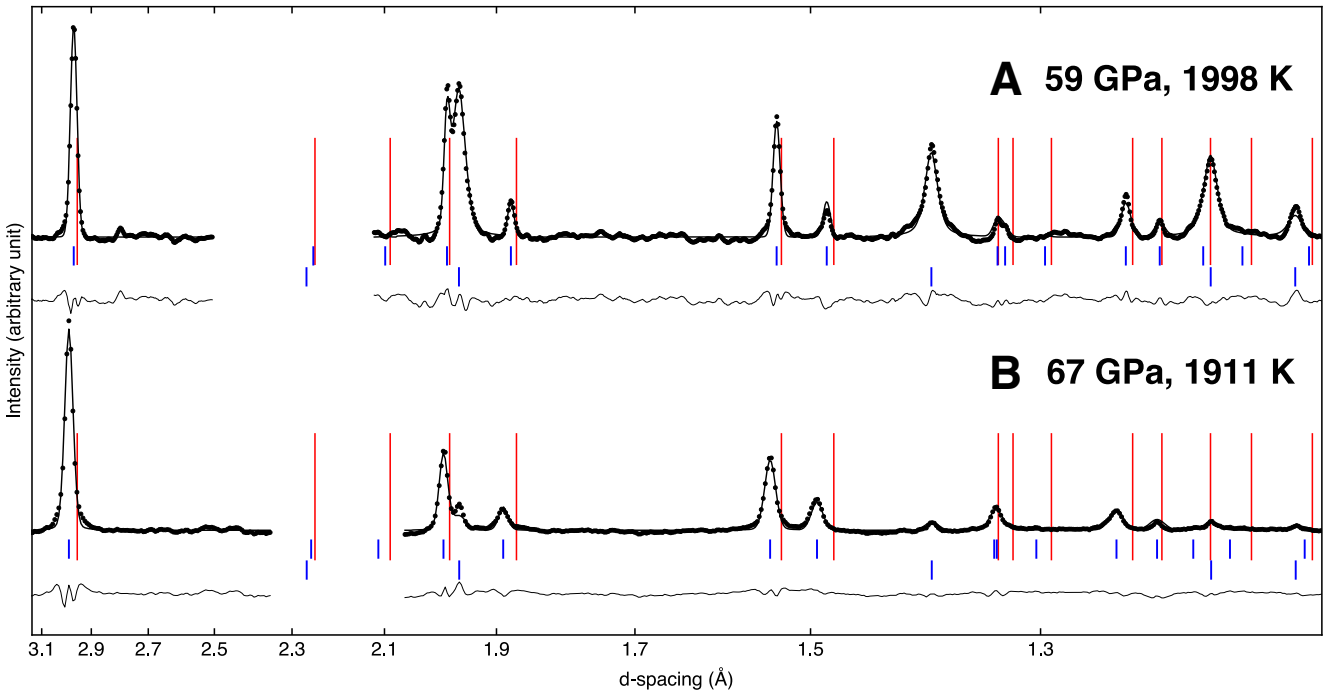

Fig. S2. **Rietveld refinements of the diffraction patterns from dense hydrous silica at 1 bar and 300 K:** **(A)** 119a and **(B)** 319 with 2.1, and 5.2 wt% H_2O, respectively (SI Tab. S1). The fit residues after background subtraction, $R_{\mathrm{wp-bknd}}$, were 1.2% and 2.3% for **(A)** and **(B)**, respectively. The black dots are the data, the solid black lines are the calculated patterns after fitting, and the thin black lines below the patterns are the difference between the fit and the observed intensities. The vertical red bars show the peak positions expected for anhydrous Stv, highlighting the systematic shifts of the observed diffraction lines. The upper and lower tick marks indicate the peak positions of hydrous Stv and the internal pressure standard and laser coupler (platinum), respectively. We did not fit a d-spacing range between 2.1 and 2.5 Å because of the severe overlap between 101_{Stv} and 111_{Pt}.

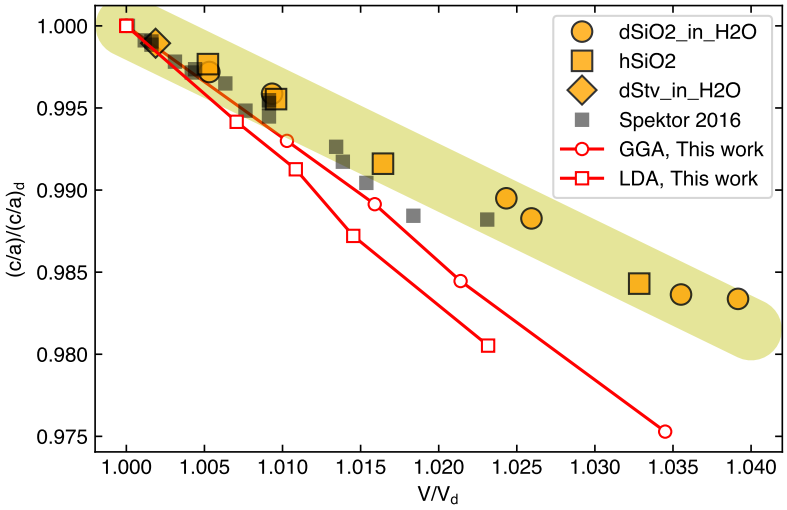

Fig. S3. The c/a ratio of the Stv recovered from hydrothermal synthesis of Ct. The yellow shapes represent different starting sample setups: dry silica glass in a H_2O medium (circles), hydrous silica gel in a Ne or Ar medium (squares), and dry Stv in a H_2O medium (diamonds). The gray squares are for hydrous Stv from a previous study (6). We also show our DFT results for comparison.

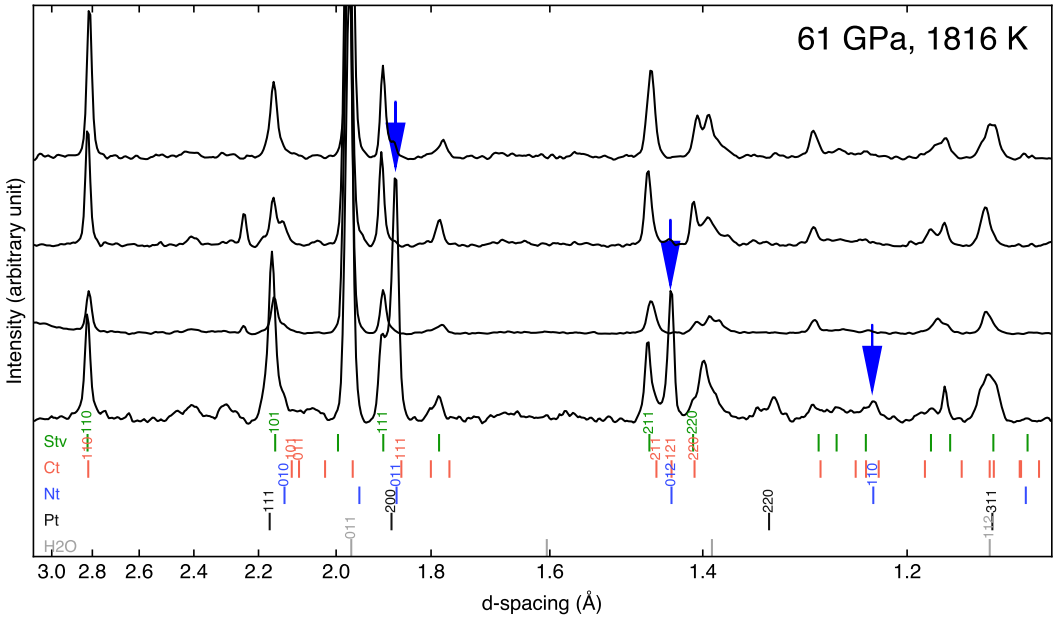

Fig. S4. X-ray diffraction patterns (wavelength 0.3344 Å) measured during heating cycle of a spot at ~61 GPa. The bars at the bottom of the diffraction patterns show the peak positions of Stv (green), Ct (orange), Nt (blue), Pt (pressure standard and laser coupler) (black), and H_2O (pressure medium) (gray). The blue arrows highlight the peak positions of the Nt phase (top: 5 minutes after the heating started; bottom: 17 minutes after the heating started). At the beginning of the heating, diffraction patterns show more features related to the Stv and Ct phases. The Stv/Ct features become weaker with heating while the Nt peaks become more intense and sharp, although they do not disappear completely in this run.

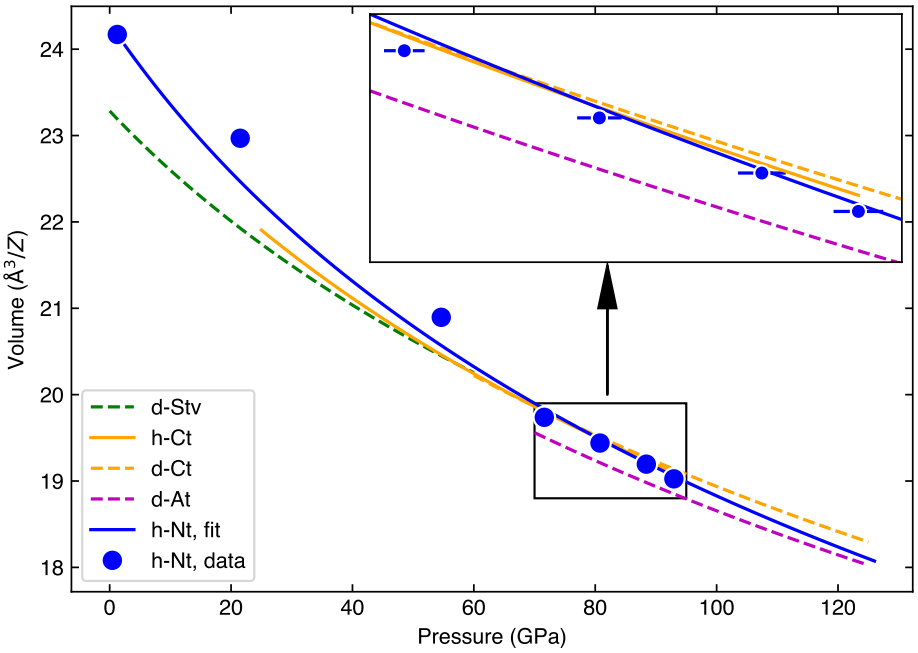

Fig. S5. Pressure–volume relations for the niccolite-type hydrous silica phase (blue solid circles) together with a fit to the Birch–Murnaghan equation (blue curve). The unit-cell volumes are normalized with respect to the number of chemical formula in a unit cell (Z). For comparison, we present the compressional curves of dry stishovite (d-Stv), dry Ct phase (d-Ct), hydrous Ct phase (h-Ct), and dry α-PbO_2 phase (d-At, seifertite) (14, 15). The inset highlights the high-pressure data.

References

1. SH Shim, *PeakPo - A python software for X-ray diffraction analysis at high pressure and high temperature. Zenodo.*, (2017).
2. C Nisr, SH Shim, K Leinenweber, A Chizmeshya, Raman spectroscopy of water-rich stishovite and dense high-pressure silica up to 55 GPa. *Am. Mineral.* **102**, 2180–2189 (2017).
3. K Spektor, et al., Ultrahydrous stishovite from high-pressure hydrothermal treatment of SiO_2. *Proc. Natl. Acad. Sci.* **108**, 20918–20922 (2011).
4. D Pearson, et al., Hydrous mantle transition zone indicated by ringwoodite included within diamond. *Nature* **507**, 221–224 (2014).
5. JR Smyth, et al., Structural systematics of hydrous ringwoodite and water in Earth's interior. *Am. Mineral.* **88**, 1402–1407 (2003).
6. K Spektor, et al., Formation of hydrous stishovite from coesite in high-pressure hydrothermal environments. *Am. Mineral.* **101**, 2514–2524 (2016).
7. T Demuth, Y Jeanvoine, J Hafner, J Angyan, Polymorphism in silica studied in the local density and generalized-gradient approximations. *J. Physics: Condens. Matter* **11**, 3833 (1999).
8. D Andrault, RJ Angel, JL Mosenfelder, TL Bihan, Equation of state of stishovite to lower mantle pressures. *Am. Mineral.* **88**, 301–307 (2003).
9. M Paterson, The determination of hydroxyl by infrared absorption in quartz, silicate glasses and similar materials. *Bull Miner.* **105**, 20–29 (1982).
10. DR Bell, GR Rossman, Water in earth's mantle: the role of nominally anhydrous minerals. *Science* **255**, 1391 (1992).
11. AR Pawley, PF McMillan, JR Holloway, Hydrogen in stishovite, with implications for mantle water content. *Science* **261**, 1024–1024 (1993).
12. P Dorogokupets, A Dewaele, Equations of state of MgO, Au, Pt, NaCl-B1, and NaCl-B2: Internally consistent high-temperature pressure scales. *High Press. Res.* **27**, 431–446 (2007).
13. WR Panero, JS Pigott, DM Reaman, JE Kabbes, Z Liu, Dry (Mg,Fe)SiO_3 perovskite in the Earth's lower mantle. *J. Geophys. Res. Solid Earth* **120**, 894–908 (2015).
14. C Nisr, et al., Phase transition and equation of state of dense hydrous silica up to 63 GPa. *J. Geophys. Res. Solid Earth* **122**, 6972–6983 (2017).
15. B Grocholski, SH Shim, V Prakapenka, Stability, metastability, and elastic properties of a dense silica polymorph, seifertite. *J. Geophys. Res. Solid Earth* **118**, 4745–4757 (2013).